PHYSICAL REVIEW FLUIDS **8**, 064302 (2023)

Mathematical model for filtration and drying in filter membranes

Hangjie Ji[1,*] and Pejman Sanaei[2,†]

[1]*Department of Mathematics, North Carolina State University, Raleigh, North Carolina 27695, USA*
[2]*Department of Mathematics and Statistics, Georgia State University, Atlanta, Georgia 30302, USA*

(Received 30 January 2023; accepted 26 May 2023; published 14 June 2023)

A filter membrane may be frequently used during its lifetime, with filtration and drying processes occurring in the porous medium for several cycles. During these cycles, the concentration and distribution of molecules or contaminants as well as the medium morphology evolve. As a consequence, the filter performance ultimately deteriorates after several cycles. In this work, we formulate a coupled mathematical model for the filtration and drying dynamics in a porous medium occurring consecutively. Our model accounts for the porous medium internal morphology (internal structure, porosity, etc.), the contaminant deposition, and the evolution of dry-fluid interfaces due to evaporation. An asymptotic model is derived based on the small aspect ratio of the thin filter membrane. The reduced model provides insights to the overall porous medium evolution over cycles of filtration and drying processes and predicts the timeline to discard the filter based on its optimum performance. Given the complexity of fluid boundary movements due to the filtration and drying processes, the reduced model still acts as an efficient prediction tool offering a tremendous reduction in computational costs.

DOI: 10.1103/PhysRevFluids.8.064302

I. INTRODUCTION

Particle deposition and solvent evaporation from porous media both play a significant role in many environmental processes and industrial applications [1]. They are essential in affecting land-atmosphere exchanges, surface energy balance, and many other biological and engineering applications [2]. An improved understanding of the contaminant transport and solvent patterns during filtration and drying processes in porous media is critical to these applications [3]. Researchers have looked into these phenomena from different perspectives, including the effects of the solvents' properties, the porous internal structure geometry and wettability on the evaporation process, as well as stages related to internal transport mechanisms that affect evaporation flux [4–7].

Generally speaking, filtration is a separation process that uses membrane filters to remove undesired particles from a fluid [8]. In typical liquid filtration problems, a fluid flows through a porous medium designed to trap solute molecules [9,10]. Depending on applications, different kinds of membrane filters can be used to sieve contaminants from the fluid [11–13].

The practical applications of filtration attracted many comprehensive works from both experimental and theoretical perspectives over the past few decades. For instance, an extensive overview of membrane separation technology [14], various fouling mechanisms during the filtration process [15], and compiling experimental and modeling results on interfacial interactions and membrane fouling [16] have been studied by the filtration community.

---

[*] hangjie_ji@ncsu.edu
[†] psanaei@gsu.edu

Filter performance is affected by a number of key design features, such as the filter thickness, internal pore structure and shape, pore connectivity, variation of pore dimensions in the depth of the filter, and the material [17,18]. Therefore, determining the filter performance and lifetime is a culmination of understanding all the fundamentals of filter behaviors, and one cannot investigate the latter without a detailed knowledge of the former. As a filtration process progresses, the particles removed from the feed solution are deposited on or in the filter. Therefore, understanding and predicting the flow and resulting fouling and behavior of the filter is a critical part of the design process. Experimental approaches are costly, and it is difficult to visualize accurately where particles are trapped in the depth of the membrane [19]. Mathematical modeling and simulation provide vital tools in helping manufacturers gain insight into filtration processes and operating conditions, thus providing a cost-effective way of optimizing filter design.

In many filtration applications, membranes are reused several times. Between any two consecutive filtration time laps (when the filtration process stops and before it starts again), the solvent evaporates from the saturated membrane. Therefore, filtration-evaporation cycles occur until the membrane performance and efficiency drop drastically. At this point, the membrane is discarded and replaced with a new one. The solvent evaporation mostly occurs from the top and bottom of the membrane. As evaporation proceeds, contaminant concentration increases, and the particles are left behind on the internal structure of the porous medium. The interplay between the transport process and contaminant deposition in the internal structure of the porous medium influences the solvent evaporation rate [20].

The topic of filtration drying of multiphase flow in porous media has been recently studied by researchers experimentally, numerically, and analytically from different points of view [21–26]. For instance, Scanziani *et al.* [27] identified a two-phase flow invasion pattern in a three-dimensional mixed-fluid porous medium (a small rock sample initially filled with oil) using time-resolved high-resolution synchrotron x-ray imaging. Their study focused on the distribution of local contact angles as water invades the pore space. Wang *et al.* [28] used the lattice Boltzmann method to investigate the effects of topological disorder and its coupling with wettability on fluid displacement in porous media by defining a disorder index to characterize disordered geometry and by reflecting the degree of fluctuation of local porosity, respectively. In 2018, Cueto-Felgueroso *et al.* [29] proposed a diffuse-interface model for the liquid-vapor flow of a van der Waals fluid in a porous medium at the pore scale. Using a simplified Darcy-Korteweg model, they investigated the dynamics of vaporization-condensation fronts under various filtration conditions and pore geometry. The works of Huinink *et al.* [30] and Panda *et al.* [31] introduced pore-scale network models for the drying processes in porous media with the presence of imposed thermal gradients. Last, Sharma and Yortso [32–34] developed several mathematical models which are formulated for the general class of problems that involve the transport of stable particulate suspensions, the processes of fines migration and fines injection, and the deep bed filtration in porous media. While extensive research has been carried out for pore-scale modeling and simulation of the drying processes in porous media, a detailed study of evaporation in porous media at the macroscopic scale is still lacking.

In this work, we first develop a continuum model for the filtration process in a filter membrane that accounts for membrane internal morphology and porosity. The membrane fouling occurs due to both particle sieving and particle adsorption operating simultaneously [9]. We also propose a different continuum model for the drying process after the filtration halts. We consider a porous material filled with a liquid solution containing molecules, and the drying process starts with a prescribed concentration. As the solvent evaporates, molecules are left behind and deposited on the membrane pore walls within the porous material. Our model tracks the interfaces between the dry and fluid regions, where the fluid evaporates from the saturated membrane. The internal membrane morphology and the particle concentration evolve due to the fluid evaporation as well as the deposition of particles within the membrane internal structure. The filtration and drying processes occur in consecutive cycles until the membrane performance deteriorates. As a result, our reduced model offers insights into the evolution of the porous medium throughout cycles of

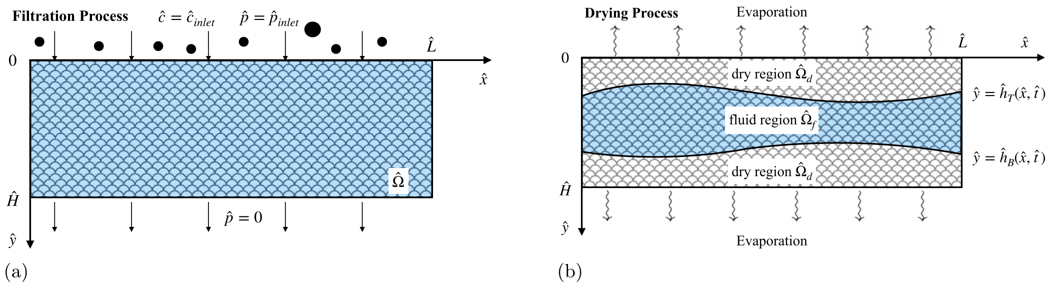

FIG. 1. Schematics of a membrane region $\hat{\Omega} = [0, \hat{L}] \times [0, \hat{H}]$. Panels (a) and (b) represent the filtration and the drying (or evaporation) processes, respectively. The filtration process takes place under constant pressure drop across the membrane, i.e., the pressure at $\hat{y} = 0$ and $\hat{y} = \hat{H}$ are prescribed as $\hat{p}_{\text{inlet}}$ and 0, respectively. Particle deposition occurs within the membrane with the inlet particle concentration being $\hat{c}_{\text{inlet}}$ at $\hat{y} = 0$. During the drying process, the domain consists of dry $\hat{\Omega}_d$ and fluid $\hat{\Omega}_f$ regions in the $\hat{x}$-$\hat{y}$ plane. $\hat{y} = \hat{h}_i(\hat{x}, \hat{t})$, $i \in \{T, B\}$ are the dry-fluid interfaces at the top and bottom of the membrane respectively, which evolve in time $\hat{t}$ due to evaporation.

filtration and drying processes, enabling us to predict the optimal timeline for replacing the filter based on its performance.

This paper is structured as follows: We introduce mathematical models for filtration and drying in a porous medium in Sec. II A and Sec. II B, respectively. We perform the nondimensionalization of the models described in Sec. II for the filtration and drying processes in Sec. III A and Sec. III B, respectively. In Sec. IV, we apply asymptotic analysis to simplify the governing equations based on the porous medium-small aspect ratio. We then summarize the simplified governing equations along with the numerical methods in Sec. V. Section VI presents the results for filtration, drying, and combined cycles of both processes. Finally, we conclude in Sec. VII with a discussion of our model and results with potential future improvements.

II. MODEL FORMULATION

We consider filtration as well as drying processes through a planar porous membrane in $(\hat{x}, \hat{y})$, as shown in Fig. 1. Note that in Sec. II, hats demonstrate the dimensional variables. We assume that the membrane is saturated with liquid during the filtration process and the solvent enters from the top of the membrane, while the fluid is stationary when evaporation occurs from the top and bottom of the membrane. The membrane region $\hat{\Omega} = [0, \hat{L}] \times [0, \hat{H}]$ consists of fluid and dry regions, $\hat{\Omega}_f$ and $\hat{\Omega}_d$, respectively. We monitor the particle concentration $\hat{c}$ as well as the membrane porosity $\hat{\phi}$ during the filtration and drying processes. The membrane properties and flow are assumed homogeneous perpendicular to the plane of the medium $\hat{\Omega}$. The membrane permeability $\hat{k}(\hat{x}, \hat{y}, \hat{t})$ is both spatial $(\hat{x}, \hat{y})$ and time $\hat{t}$ dependent. We note that even if the permeability is initially uniform, fouling and particle deposition will lead to nonuniformities over time.

A. Filtration

In this section, we consider the filtration process through the membrane as shown in Fig. 1(a). The flow can be modelled by Darcy's law [9,17]. The superficial Darcy velocity $\hat{\boldsymbol{u}} = (\hat{u}, \hat{v})$ within the membrane is then given in terms of the pressure $\hat{p}$ by

$$\hat{\boldsymbol{u}} = -\frac{\hat{k}}{\hat{\mu}} \hat{\nabla} \hat{p}, \quad \hat{\nabla} \cdot \hat{\boldsymbol{u}} = 0, \quad \text{in} \quad \hat{\Omega}, \tag{1}$$

where $\hat{\nabla} = (\frac{\partial}{\partial \hat{x}}, \frac{\partial}{\partial \hat{y}})$ and $\hat{\mu}$ is the viscosity of the fluid [35]. The membrane permeability $\hat{k}(\hat{x}, \hat{y}, \hat{t})$ must be linked to membrane characteristics, which evolve in time due to fouling. Filtration commonly takes place under one of two scenarios: specified flux or pressure drop. In this paper, we only focus on the latter case; however, our model can be readily extended to the specified flux scenario. For a constant applied pressure drop, the conditions applied at the upstream and downstream membrane surfaces, $\hat{y} = 0, \hat{H}$, as well as the left and right walls, $\hat{x} = 0, \hat{L}$, are

$$\hat{p}|_{\hat{y}=0} = \hat{p}_{\text{inlet}}, \quad \hat{p}|_{\hat{y}=\hat{H}} = 0, \quad \left.\frac{\partial \hat{p}}{\partial \hat{x}}\right|_{\hat{x}=0,\,\hat{L}} = 0. \tag{2}$$

We use the Kozeny-Carman model [35] to describe the membrane permeability $\hat{k}$ as a function of the local membrane porosity or void fraction $\hat{\phi}(\hat{x}, \hat{y}, \hat{t})$:

$$\hat{k} = \frac{\hat{\chi}\hat{\phi}^3}{(1-\hat{\phi})^2}, \quad \text{in} \quad \hat{\Omega}, \tag{3}$$

where $\hat{\chi}$ is the Kozeny coefficient (with dimensions of length squared, as for permeability). Porosity $\hat{\phi}(\hat{x}, \hat{y}, \hat{t}) \in (0, 1)$ is the local pore volume fraction in any small membrane element at $(\hat{x}, \hat{y})$ and time $\hat{t}$. The superficial Darcy velocity $\hat{\boldsymbol{u}}$ is the fluid velocity averaged [locally, at $(\hat{x}, \hat{y})$] over both membrane and pore volume, which differs from the actual mean velocity of the fluid within the membrane pores [denoted by $\hat{\boldsymbol{u}}_f$ and averaged over the pore cross-section at $(\hat{x}, \hat{y})$]. The membrane porosity links $\hat{\boldsymbol{u}}_f$ and $\hat{\boldsymbol{u}}$ via

$$\hat{\boldsymbol{u}} = \hat{\phi}\hat{\boldsymbol{u}}_f, \quad \text{in} \quad \hat{\Omega}. \tag{4}$$

The mass transport of the particles in the feed through the membrane is described by an advection-dispersion-reaction equation,

$$\frac{\partial(\hat{\phi}\hat{c})}{\partial \hat{t}} + \hat{\nabla} \cdot (\hat{\boldsymbol{u}}_f(\hat{\phi}\hat{c})) = \hat{\nabla} \cdot [\hat{\Xi}\hat{\nabla}(\hat{\phi}\hat{c})] - \hat{f}_f(\hat{\boldsymbol{u}}, \hat{\phi}, \hat{c}), \quad \text{in} \quad \hat{\Omega}, \tag{5}$$

where $\hat{c}(\hat{x}, \hat{y}, \hat{t})$ is the concentration of particles per unit volume of fluid in the membrane, $\hat{\Xi}$ is the dispersion coefficient of particles in the feed suspension (here assumed constant), and $\hat{f}_f(\hat{\boldsymbol{u}}, \hat{\phi}, \hat{c})$ is the deposition function for the filtration process, which models how particles carried by the feed are deposited locally within the membrane and depends on the Darcy velocity, membrane porosity, and local particle concentration. Note that here we adopt the general advection-dispersion-reaction equation for the particle concentration within the porous medium as shown in (5). However, in Sec. III and Sec. IV we carry out further analysis and after nondimensionalization and applying the asymptotic analysis respectively, the dispersion term is dropped as shown in (43) and discussed by Sharma and Yortso [32–34]. The reason we keep the dispersion term in (5) is due to some application that might be of interest. Practically, in a slow filtration process, or during the late stages of filtration when the flow rate is naturally very low due to a high level of fouling, the particle effective dispersion might play an important role. The initial particle concentration within the membrane for the filtration process is prescribed by

$$\hat{c}|_{\hat{t}=0} = \hat{c}_{f_{\text{initial}}}, \quad \text{in} \quad \hat{\Omega}. \tag{6}$$

We assume the particle concentration is constant at the membrane inlet and the mass flux of particles continuous across the membrane outlet [9,36,37], as well as the left and right walls, i.e.,

$$\hat{c}|_{\hat{y}=0} = \hat{c}_{\text{inlet}}, \quad \left.\frac{\partial(\hat{\phi}\hat{c})}{\partial \hat{y}}\right|_{\hat{y}=\hat{H}} = 0, \quad \left.\frac{\partial(\hat{\phi}\hat{c})}{\partial \hat{x}}\right|_{\hat{x}=0,\,\hat{L}} = 0. \tag{7}$$

The membrane porosity decreases as particles are deposited within the membrane on the pore walls. We assume this occurs at a rate proportional to the deposition function $\hat{f}_f(\hat{\boldsymbol{u}}, \hat{\phi}, \hat{c})$, hence,

$$\frac{\partial \hat{\phi}}{\partial \hat{t}} = -\hat{\alpha}_f \hat{f}_f(\hat{\boldsymbol{u}}, \hat{\phi}, \hat{c}), \quad \text{in} \quad \hat{\Omega}, \tag{8}$$

where $\hat{\alpha}_f$ is a constant specific to the particular membrane/feed system or pore shrinkage coefficient, with dimensions of volume (inverse of concentration). We solve (8) subject to a specified initial porosity profile,

$$\hat{\phi}(\hat{x},\hat{y},0)=\hat{\phi}_{f_{\text{initial}}}(\hat{x},\hat{y}),\quad \text{in}\quad \hat{\Omega}. \tag{9}$$

The model is closed by specifying the deposition function $\hat{f}_f(\hat{\boldsymbol{u}},\hat{\phi},\hat{c})$. We consider two distinct mechanisms for particle deposition: (i) adsorption (particles much smaller than the membrane pores are deposited onto the pore walls, shrinking pores and thus reducing the local porosity) and (ii) blocking (particles larger than the local membrane pore size get stuck and block the pore inlet). These two components will be modeled independently [9].

To propose a reasonable choice for $\hat{f}_f(\hat{\boldsymbol{u}},\hat{\phi},\hat{c})$, consider a membrane with cylindrical pores of radius $\hat{r}$ contained within lattices of fixed size. For the adsorption, we note that the rate at which the particles arrive at the pore wall (and thus adhere) should be proportional to the local particle concentration and pore surface area; therefore we propose an adsorption rate proportional to $\hat{\phi}^{\frac{1}{2}}\hat{c}$. Here we note that for the proposed membrane structure, the pore surface area scales with $\hat{\phi}^{\frac{1}{2}}$, since $\hat{\phi}\sim(\frac{\hat{r}}{\text{lattice cross sectional size}})^2$. In this model, we assume that adsorption simply requires that small particles in the vicinity of the wall deposit onto it. The rate at which this happens is assumed to depend primarily on the local concentration, independently of the local flow velocity. For blocking, we require a large particle, bigger than the local pore size, to arrive and block the pore from above, and hence we anticipate blocking to proceed at a rate proportional to the local advective flux of particles $|\hat{\boldsymbol{u}}|\hat{c}$ (large particles can either pass through a pore or they cannot: The more that pass a location, the greater the blocking rate). Noting that pore radius scales with $\hat{\phi}^{\frac{1}{2}}$, with the above assumptions blocking will also be proportional to $(1-\hat{\phi}^{\frac{1}{2}})$ (smaller pores are more readily blocked). Hence, the blocking term is proportional to $|\hat{\boldsymbol{u}}|(1-\hat{\phi}^{\frac{1}{2}})\hat{c}$, and the deposition function $\hat{f}_f(\hat{\boldsymbol{u}},\hat{\phi},\hat{c})$ is taken as

$$\hat{f}_f(\hat{\boldsymbol{u}},\hat{\phi},\hat{c})=\underbrace{\hat{\lambda}_f\hat{\phi}^{\frac{1}{2}}\hat{c}}_{\text{adsorption}}+\underbrace{\hat{\delta}_f|\hat{\boldsymbol{u}}|\big(1-\hat{\phi}^{\frac{1}{2}}\big)\hat{c}}_{\text{blocking}}, \tag{10}$$

where $\hat{\lambda}_f\geqslant 0$ is the average adsorption rate of particles, relating to the physics of the attraction between particles and pore wall, and $\hat{\delta}_f\geqslant 0$ is the average blocking coefficient, with dimensions of inverse length (in the absence of adsorption, $1/\hat{\delta}_f$ gives a measure of the penetration depth of blocking particles into the porous medium). The model assumes implicitly that particle sizes are uniformly distributed and that all particles can enter the membrane and thus can be deposited within it by either adsorption or blocking fouling modes. According to the proposed model, blocking will dominate at high fluxes, while adsorption is more important in a low-flux scenario. The effect of changing porosity on the blocking behavior is inherent in the model. As pore constriction occurs and porous medium resistance increases, the mean velocity of the fluid within pores decreases. The changes in fluid velocity and porosity are both reflected in the blocking model, as explained by (5)–(10).

In order to evaluate the performance of model filter membranes, we define two quantities which are the common experimental characterization of filter membrane performance. The total dimensional volumetric flux $\hat{Q}(\hat{t})$ through the membrane filter is given by

$$\hat{Q}(\hat{t})=\int_0^{\hat{L}}|\hat{\boldsymbol{u}}_f(\hat{x},\hat{H},\hat{t})|\,d\hat{x}, \tag{11}$$

and the volumetric throughput $\hat{V}(\hat{t})$ represents the total cumulative volume of filtrate processed by time $\hat{t}$, is defined as the time integral of the volumetric flux $\hat{Q}(\hat{t})$:

$$\hat{V}(\hat{t})=\int_0^{\hat{t}}\hat{Q}(\hat{t}')\,d\hat{t}'. \tag{12}$$

B. Drying

We now present a model for the drying process as shown in Fig. 1(b). We assume that the porous medium is saturated with stationary liquid, and the evaporation occurs from the top and bottom of the membrane, i.e., $\hat{y} = 0$ and $\hat{y} = \hat{H}$, respectively. The interfaces between the dry and fluid regions are located at $\hat{y} = \hat{h}_T(\hat{x}, \hat{t})$ and $\hat{y} = \hat{h}_B(\hat{x}, \hat{t})$ for the top and bottom of the membrane respectively, which we expect to be nontrivial, as the membrane porosity $\hat{\phi}(\hat{x}, \hat{y})$ evolves in time nonuniformly (this will be explained in details below). As time evolves, the particle concentration in the fluid region changes due to (i) evaporation at $\hat{y} = \hat{h}_i(\hat{x}, \hat{t})$, $i \in \{T, B\}$ and (ii) deposition of particles on the membrane internal structure. We assume there is no effective flow in the fluid region during the drying process, and therefore the particle concentration in the fluid region follows a reaction-dispersion equation,

$$\frac{\partial(\hat{\phi}\hat{c})}{\partial\hat{t}} = \hat{\nabla}\cdot[\hat{\Xi}\hat{\nabla}(\hat{\phi}\hat{c})] - \hat{f}_d(\hat{\phi}, \hat{c}), \quad \text{in} \quad \hat{\Omega}_f, \tag{13}$$

where $\hat{f}_d(\hat{\phi}, \hat{c})$ is the deposition function for the drying process. Here $\hat{f}_d(\hat{\phi}, \hat{c})$ depends on the porosity and local particle concentration and models how particles are deposited locally within the membrane [17,37]. The initial particle concentration within the membrane for the drying process is prescribed by

$$\hat{c}|_{\hat{t}=0} = \hat{c}_{d_{\text{initial}}}, \quad \text{in} \quad \hat{\Omega}_f. \tag{14}$$

We apply no flux of particles at the left and right walls of the fluid region, i.e.,

$$\left.\frac{\partial(\hat{\phi}\hat{c})}{\partial\hat{x}}\right|_{\hat{x}=0,\hat{L}} = 0. \tag{15}$$

Since we assume the flow is static and there is no effective flow in the fluid region during the drying process, the particle concentration in the fluid region follows the reaction-dispersion equation. Therefore, the evaporation is related to the dispersion-driven particle deposition at the dry-fluid interfaces. In other words, at the dry-fluid interfaces, the particle deposition, which only happens due to particle dispersion, is proportional to the evaporation rate, porosity, and particle concentration. Therefore, the boundary condition at the dry-fluid region interfaces, where evaporation occurs, is

$$\hat{\Xi}\hat{\nabla}(\hat{\phi}\hat{c})\cdot\boldsymbol{n}_i|_{\hat{y}=\hat{h}_i(\hat{x})} = -\hat{\gamma}_d\hat{E}\hat{\phi}\hat{c}|_{\hat{y}=\hat{h}_i(\hat{x})}, \quad i \in \{T, B\}, \tag{16}$$

where $\hat{\gamma}_d$ is a dimensionless scaling parameter for the particle deposition rate and it is related to the properties of the particles and solvent, $\hat{E}(\hat{\phi}, \hat{c})$ is the evaporation flux, and $\boldsymbol{n}_i$ is the outward unit normal on the interface pointing out of the fluid.

The evolution of the dry-fluid interfaces $\hat{y} = \hat{h}_i(\hat{x}, \hat{t})$, $i \in \{T, B\}$ is driven by the solvent evaporation,

$$\frac{\partial\hat{h}_T}{\partial\hat{t}} = \hat{E}(\hat{\phi}, \hat{c}), \quad \hat{h}_T|_{\hat{t}=0} = 0, \quad \frac{\partial\hat{h}_B}{\partial\hat{t}} = -\hat{E}(\hat{\phi}, \hat{c}), \quad \hat{h}_B|_{\hat{t}=0} = \hat{H}, \tag{17}$$

where the different signs in the equations arise from the direction of evaporative fluxes at the top and bottom interfaces [see Fig. 1(b)]. The evaporation rate of the solvent depends on many factors such as the liquid temperature, the pressure difference at the liquid-gas interface, intermolecular forces, and the relative humidity in the surrounding air. A commonly used model for evaporation flux can be written as [38–41]

$$\hat{E} = \hat{\alpha}_v\frac{\hat{\rho}_v}{\hat{\rho}_l}\left(\frac{\hat{R}_g\hat{T}_{\text{sat}}}{2\pi}\right)^{1/2}\left(\frac{\hat{p}_{\text{ve}}}{\hat{p}_v} - 1\right), \tag{18}$$

where the nonequilibrium interfacial condition at the gas-liquid (in our case dry-fluid) interfaces $\hat{y} = \hat{h}_i(\hat{x}, \hat{t})$, $i \in \{T, B\}$ gives [38–40]

$$\frac{\hat{p}_{\mathrm{ve}}}{\hat{p}_v} - 1 = \frac{\hat{p}_l - \hat{p}_v}{\hat{\rho}_l \hat{R}_g \hat{T}_{\mathrm{sat}}} + \frac{\hat{L}_v}{\hat{R}_g \hat{T}_{\mathrm{sat}}} \left(\frac{\hat{T}|_{\hat{h}}}{\hat{T}_{\mathrm{sat}}} - 1 \right), \tag{19}$$

where $\hat{\alpha}_v$ is an accommodation coefficient for evaporation, $\hat{p}_v$ is the vapor pressure, $\hat{p}_l$ is the fluid pressure at the interface, $\hat{p}_{\mathrm{ve}}$ is the equilibrium vapor pressure, $\hat{R}_g$ is the specific gas constant, $\hat{T}_{\mathrm{sat}}$ is the equilibrium saturation temperature, $\hat{L}_v$ is the specific internal latent heat of vaporization, and $\hat{T}|_{\hat{h}}$ is the interfacial temperature at the dry-fluid interfaces. The work by Karapetsa *et al.* [40] used $\hat{\alpha}_v$ to account for the influence of interfacial surfactant concentration on the evaporation rate.

In the present work, the evaporative flux depends on both the particle concentration $\hat{c}$ and porosity $\hat{\phi}$ at the dry-fluid interfaces. The particle at the dry-fluid interfaces hinders evaporation, and the solid in the porous medium acts as a barrier to local evaporation. To account for these effects, we model the accommodation coefficient as

$$\hat{\alpha}_v(\hat{\phi}, \hat{c}) = \frac{\hat{\phi}\hat{c}_{\mathrm{sat}}}{\hat{c}_{\mathrm{sat}} + \hat{\Psi}\hat{c}}, \tag{20}$$

where $\hat{c}_{\mathrm{sat}}$ is the saturation particle concentration in the solvent, and the dimensionless constant $\hat{\Psi} > 0$ scales the importance of the particle concentration to the evaporation effects. Moreover, we assume that the interfacial temperature $\hat{T}|_{\hat{y}=\hat{h}_i} = \hat{T}_{\mathrm{sat}}$, and the liquid-vapor pressure difference $\Delta\hat{p} = \hat{p}_l - \hat{p}_v > 0$ at the interface is constant. Combining (18)–(20) yields a simplified model for the evaporation flux

$$\hat{E}(\hat{\phi}, \hat{c}) = \frac{\hat{\eta}_d \hat{\phi} \hat{c}_{\mathrm{sat}}}{\hat{c}_{\mathrm{sat}} + \hat{\Psi}\hat{c}}, \quad \hat{\eta}_d = \frac{\hat{\rho}_v \Delta\hat{p}}{\hat{\rho}_l^2 (2\pi \hat{R}_g \hat{T}_{\mathrm{sat}})^{1/2}}, \tag{21}$$

where $\hat{E}(\hat{\phi}, \hat{c})$ depends on ambient vapor pressure, temperature, and liquid properties. For the low particle concentration limit, $\hat{\Psi}\hat{c} \ll \hat{c}_{\mathrm{sat}}$, the evaporative flux $\hat{E}$ approaches $\hat{\eta}_d\hat{\phi}$, which highlights the impact of membrane porosity on the evaporation. In this simplified model, we focus on the influence of porosity $\hat{\phi}$ and particle concentration $\hat{c}$ on evaporation. Both the temperature field in the liquid and the relative humidity near the evaporation fronts are assumed spatially uniform. Our model also does not include the influences of surface tension and the wettability of the material. We note that the one-sided evaporation model we use does not consider the impact of liquid evaporation on the dynamics of the gas phase near the free surface. This differs from the approach taken by Mahadevan *et al.* [42,43], who utilized a two-phase model to describe the evaporation occurring in porous media due to saturated or dry gas flow through the media.

We assume that the membrane porosity decreases as particles are deposited within the internal structure of the membrane, i.e.,

$$\frac{\partial\hat{\phi}}{\partial\hat{t}} = -\hat{\alpha}_d \hat{f}_d(\hat{\phi}, \hat{c}), \quad \text{in} \quad \hat{\Omega}_f, \tag{22}$$

subject to a specified initial porosity profile for the drying process,

$$\hat{\phi}(\hat{x}, \hat{y}, 0) = \hat{\phi}_{d_{\mathrm{initial}}}(\hat{x}, \hat{y}), \quad \text{in} \quad \hat{\Omega}_f, \tag{23}$$

where $\hat{\alpha}_d$ is the pore shrinkage coefficient and $\hat{f}_d$ is the deposition function for the drying process,

$$\hat{f}_d(\hat{\phi}, \hat{c}) = \hat{\lambda}_d \hat{\phi}^{\frac{1}{2}} (\hat{c} - \hat{c}_{\mathrm{sat}})_+. \tag{24}$$

Here $\hat{\lambda}_d$ is the average deposition rate of particles relating to the physics of the attraction between particles and pore wall, $\hat{c}_{\mathrm{sat}}$ represents the saturation concentration of particles, and $(\hat{c} - \hat{c}_{\mathrm{sat}})_+ = \max\{\hat{c} - \hat{c}_{\mathrm{sat}}, 0\}$. Similarly to what we explained in Sec. II A, if we consider a membrane with cylindrical pores of radius r contained within lattices of fixed size, then we can assume the rate of particles arriving at the pore wall should be proportional to pore surface area as well as the difference between the local particle concentration and the saturation particle concentration [9]. Note that for the proposed membrane structure, the pore surface area scales with $\hat{\phi}^{\frac{1}{2}}$. Therefore, the adsorption rate is proportional to $\hat{\phi}^{\frac{1}{2}}(\hat{c}-\hat{c}_{\text{sat}})_{+}$, and we propose (24) for $\hat{f}_d(\hat{\phi},\hat{c})$.

III. NONDIMENSIONALIZATION

To reduce the number of independent parameters, we nondimensionalize the models for the (i) filtration and (ii) drying processes described in Sec. II A and Sec. II B respectively, using appropriate scalings introduced for each one below. Recall that the membrane is thin with a small aspect ratio, i.e., $\epsilon = \hat{H}/\hat{L} \ll 1$.

A. Filtration

We use the following scalings to nondimensionalize the model given (1)–(12) in Sec. II B,

$$(\hat{x},\hat{y}) = \hat{L}(x,\epsilon y), \quad \hat{p} = \hat{p}_{\text{inlet}}p, \quad \hat{\phi} = \phi, \quad (\hat{\boldsymbol{u}},\hat{\boldsymbol{u}}_f) = \frac{\hat{\chi}\hat{p}_{\text{inlet}}}{\epsilon\hat{L}\hat{\mu}}(\boldsymbol{u},\boldsymbol{u}_f), \quad \hat{c} = \hat{c}_{\text{inlet}}c,$$

$$\hat{k} = \hat{\chi}k, \quad \hat{t} = \frac{\epsilon\hat{L}\hat{\mu}}{\hat{\alpha}_f\hat{\delta}_f\hat{\chi}\hat{p}_{\text{inlet}}\hat{c}_{\text{inlet}}}t, \quad \hat{\mathcal{Q}} = \frac{\hat{\chi}\hat{p}_{\text{inlet}}}{\epsilon\hat{\mu}}\mathcal{Q}, \quad \hat{\mathcal{V}} = \frac{\hat{L}}{\hat{\alpha}_f\hat{\delta}_f\hat{c}_{\text{inlet}}}\mathcal{V}, \quad T_f = \epsilon\hat{L}\hat{\alpha}_f\hat{\delta}_f\hat{c}_{\text{inlet}},$$

$$\text{Pe} = \frac{\hat{\chi}\hat{p}_{\text{inlet}}}{\hat{\Xi}\hat{\mu}}, \quad \lambda_f = \frac{\epsilon^2\hat{L}^2\hat{\mu}\hat{\lambda}_f}{\hat{\chi}\hat{p}_{\text{inlet}}}, \quad \delta_f = \epsilon\hat{L}\hat{\delta}_f, \quad \alpha_f = \frac{\epsilon\hat{L}\hat{\mu}\hat{\lambda}_f}{\hat{\delta}_f\hat{\chi}\hat{p}_{\text{inlet}}} = \frac{\lambda_f}{\delta_f}, \tag{25}$$

where $\boldsymbol{u} = (u,v)$ and $\boldsymbol{u}_f = (u_f,v_f)$ are the dimensionless Darcy velocity and the actual mean velocity of fluid within the membrane pores, respectively. Using these scalings, from (1)–(12) we obtain the dimensionless model for the filtration process as

$$u = -\epsilon k\frac{\partial p}{\partial x}, \quad v = -k\frac{\partial p}{\partial y}, \quad \epsilon\frac{\partial u}{\partial x} + \frac{\partial v}{\partial y} = 0, \quad p|_{y=0} = 1, \quad p|_{y=1} = 0, \tag{26}$$

$$k = \frac{\phi^3}{(1-\phi)^2}, \tag{27}$$

$$\boldsymbol{u} = \phi\boldsymbol{u}_f, \tag{28}$$

$$T_f\frac{\partial(\phi c)}{\partial t} + \epsilon u\frac{\partial c}{\partial x} + v\frac{\partial c}{\partial y} = \frac{1}{\text{Pe}}\left[\epsilon^2\frac{\partial^2(\phi c)}{\partial x^2} + \frac{\partial^2(\phi c)}{\partial y^2}\right] - \lambda_f\phi^{\frac{1}{2}}c - \delta_f|\boldsymbol{u}|\big(1-\phi^{\frac{1}{2}}\big)c, \tag{29}$$

$$c|_{t=0} = c_{f_{\text{initial}}}, \quad c|_{y=0} = 1, \quad \left.\frac{\partial(\phi c)}{\partial y}\right|_{y=1} = 0, \quad \left.\frac{\partial(\phi c)}{\partial x}\right|_{x=0,1} = 0, \tag{30}$$

$$\frac{\partial\phi}{\partial t} = -\alpha_f\phi^{\frac{1}{2}}c - |\boldsymbol{u}|\big(1-\phi^{\frac{1}{2}}\big)c, \quad \phi(x,y,0) = \phi_{f_{\text{initial}}}(x,y), \tag{31}$$

$$\mathcal{Q} = \int_0^1 |\boldsymbol{u}_f|\,dx, \quad \mathcal{V} = \int_0^t \mathcal{Q}\,dt'. \tag{32}$$

B. Drying

In order to nondimensionalize the model (13)–(24) presented in Sec. II B, we use (25) along with new scalings

$$\hat{c}_{\text{sat}} = \hat{c}_{\text{inlet}}c_{\text{sat}}, \quad \hat{h}_i = \epsilon\hat{L}h_i, \quad i\in\{T,B\}, \quad \hat{E} = \hat{\eta}_d E, \quad T_d = \frac{\epsilon\hat{L}\hat{\alpha}_f\hat{\delta}_f\hat{\chi}\hat{p}_{\text{inlet}}\hat{c}_{\text{inlet}}}{\hat{\Xi}\hat{\mu}},$$

$$\lambda_d = \frac{\epsilon^2\hat{L}^2\hat{\lambda}_d}{\hat{\Xi}}, \quad \gamma_d = \frac{\epsilon\hat{L}\hat{\gamma}_d\hat{\eta}_d}{\hat{\Xi}}, \quad \eta_d = \frac{\hat{\mu}\hat{\eta}_d}{\hat{\alpha}_f\hat{\delta}_f\hat{\chi}\hat{p}_{\text{inlet}}\hat{c}_{\text{inlet}}}, \quad \alpha_d = \frac{\epsilon\hat{L}\hat{\mu}\hat{\alpha}_d\hat{\lambda}_d}{\hat{\alpha}_f\hat{\delta}_f\hat{\chi}\hat{p}_{\text{inlet}}}, \quad \Psi = \frac{\hat{\Psi}\hat{c}_{\text{inlet}}}{\hat{c}_{\text{sat}}}, \tag{33}$$

to obtain the nondimensional equations

$$T_d \frac{\partial(\phi c)}{\partial t} = \epsilon^2 \frac{\partial^2(\phi c)}{\partial x^2} + \frac{\partial^2(\phi c)}{\partial y^2} - \lambda_d \phi^{\frac{1}{2}}(c - c_{\text{sat}})_+, \quad c|_{t=0} = c_{d_{\text{initial}}}, \quad \left.\frac{\partial(\phi c)}{\partial x}\right|_{x=0,1} = 0, \tag{34}$$

$$\frac{1}{\sqrt{1+\epsilon^2\left(\frac{\partial h_i}{\partial x}\right)^2}} \left.\left[-\epsilon^2 \frac{\partial(\phi c)}{\partial x}\frac{\partial h_i}{\partial x} + \frac{\partial(\phi c)}{\partial y}\right]\right|_{y=h_i(x)} = \pm \gamma_d E \phi c|_{y=h_i(x)}, \quad i \in \{T, B\}, \tag{35}$$

$$\frac{\partial h_T}{\partial t} = \eta_d E, \quad h_T|_{t=0} = 0, \quad \frac{\partial h_T}{\partial t} = -\eta_d E, \quad h_B|_{t=0} = 1, \tag{36}$$

$$E(\phi, c) = \frac{\phi}{1 + \Psi c}, \tag{37}$$

$$\frac{\partial \phi}{\partial t} = -\alpha_d \phi^{\frac{1}{2}}(c - c_{\text{sat}})_+, \quad \phi(x, y, 0) = \phi_{d_{\text{initial}}}(x, y). \tag{38}$$

Note that to obtain (35), we use the unit normal vectors at the dry-fluid interfaces given by $\boldsymbol{n}_T = -\frac{(-\epsilon\frac{\partial h_T}{\partial x},1)}{\sqrt{1+\epsilon^2(\frac{\partial h_T}{\partial x})^2}}$ and $\boldsymbol{n}_B = \frac{(-\epsilon\frac{\partial h_B}{\partial x},1)}{\sqrt{1+\epsilon^2(\frac{\partial h_B}{\partial x})^2}}$.

IV. ASYMPTOTIC ANALYSIS

The complete dimensionless system described in Sec. III is extremely hard to solve analytically, and it is also computationally costly to solve numerically in a brute-force way. Therefore, we make use of the fact that the membrane aspect ratio $\epsilon = \hat{H}/\hat{L} \ll 1$. This allows us to achieve a simpler, computationally feasible, reduced asymptotic model. Below, we asymptotically expand the variables u, v, u_f, v_f, k, ϕ, c, h_i (for $i \in \{T, B\}$), E, $\mathcal{Q}$, and $\mathcal{V}$ in the form of

$$i = i_0 + \epsilon i_1 + \epsilon^2 i_2 + \mathcal{O}(\epsilon^3). \tag{39}$$

Note that there are four timescales in the model: a short timescale based on the flow transit time across the membrane during the filtration process [see (5)], and three longer timescales, on which the particle deposition occurs in both filtration and dying processes [see (8) and (22)] and the dry-fluid interfaces evolve during the drying process [see (17)]. For the filtration process, since our investigation primarily concerns the long-time fouling due to particle deposition, we assume that the flow adapts quasistatically to the changing of porosity and set $T_f = \mathcal{O}(\epsilon)$ in our analysis for the timescale given in (25). We will present the leading-order model for the filtration process in Sec. IV A. For the drying process discussed in Sec. IV B, since there is no effective flow, we will first consider the case $T_d = \mathcal{O}(1)$ in (33) so that the particle concentration in the fluid region continuously evolves and is driven by both particle deposition and dispersion. We will also discuss the particle deposition-limited regime where $T_d \gg 1$ and the dispersion is negligible.

A. Filtration

With the quasistatic assumption [$T_f = \mathcal{O}(\epsilon)$] as well as assuming $\text{Pe} = \mathcal{O}(\epsilon^{-1})$ (as shown in Table II), (26)–(32) along with the asymptotic expansions (39) yield the leading-order model for the filtration process in the membrane region Ω as

$$u_0 = 0, \quad v_0 = -k_0 \frac{\partial p_0}{\partial y}, \quad \frac{\partial v_0}{\partial y} = 0, \quad p_0|_{y=0} = 1, \quad p_0|_{y=1} = 0, \tag{40}$$

$$k_0 = \frac{\phi_0^3}{(1 - \phi_0)^2}, \tag{41}$$

$$u_{f_0} = 0, \quad v_0 = \phi v_{f_0}, \tag{42}$$

$$v_0 \frac{\partial c_0}{\partial y} = -\lambda_f \phi_0^{\frac{1}{2}} c_0 - \delta_f v_0 \big(1 - \phi_0^{\frac{1}{2}}\big) c_0, \tag{43}$$

$$c_0|_{t=0} = c_{f_{\text{initial}}}, \quad c_0|_{y=0} = 1, \quad \left.\frac{\partial(\phi_0 c_0)}{\partial y}\right|_{y=1} = 0, \tag{44}$$

$$\frac{\partial \phi_0}{\partial t} = -\alpha_f \phi_0^{\frac{1}{2}} c_0 - v_0 \big(1 - \phi_0^{\frac{1}{2}}\big) c_0, \quad \phi_0(x, y, 0) = \phi_{\text{initial}}(x, y), \tag{45}$$

$$\mathcal{Q}_0 = \int_0^1 |v_0|\, dx, \quad \mathcal{V}_0 = \int_0^t \mathcal{Q}_0\, dt'. \tag{46}$$

B. Drying

To simplify the governing equations for the drying dynamics, we first define the effective particle concentration as $\beta_0 = \phi_0 c_0$. The system (34)–(38), along with the asymptotic expansions (39), reduces to the leading-order model for the drying process in the fluid region $\Omega_f = \{(x, y)\,|\, 0 < x < 1,\ h_{T_0}(x, t) \leqslant y \leqslant h_{B_0}(x, t)\}$ as

$$T_d \frac{\partial \beta_0}{\partial t} = \frac{\partial^2 \beta_0}{\partial y^2} - \lambda_d \phi^{\frac{1}{2}} \left(\frac{\beta_0}{\phi_0} - c_{\text{sat}}\right)_+, \quad \beta_0|_{t=0} = \beta_{d_{\text{initial}}} = \phi_{d_{\text{initial}}} c_{d_{\text{initial}}}, \tag{47}$$

$$\left.\frac{\partial \beta_0}{\partial y}\right|_{y=h_{i_0}(x)} = \pm \gamma_d E_0 \beta_0, \quad i \in \{T, B\}, \tag{48}$$

$$\frac{\partial h_{T_0}}{\partial t} = \eta_d E_0, \quad h_{T_0}|_{t=0} = 0, \quad \frac{\partial h_{B_0}}{\partial t} = -\eta_d E_0, \quad h_{B_0}|_{t=0} = 1, \tag{49}$$

$$E_0 = \frac{\phi_0^2}{\phi_0 + \Psi \beta_0}, \tag{50}$$

$$\frac{\partial \phi_0}{\partial t} = -\alpha_d \phi_0^{\frac{1}{2}} \left(\frac{\beta_0}{\phi_0} - c_{\text{sat}}\right)_+, \quad \phi_0|_{t=0} = \phi_{d_{\text{initial}}}. \tag{51}$$

V. SUMMARY AND NUMERICAL METHOD

In this section, we summarize the model given in Sec. IV and discuss the numerical method to solve them. For brevity, we drop the subscript “0” from the variables.

A. Filtration

From (40) and (41), we obtain the leading order of the Darcy velocity in y-direction $v(x, t)$ as

$$v = \left[\int_0^1 \frac{(1-\phi)^2}{\phi^3} dy\right]^{-1}. \tag{52}$$

Then we solve (43) for the particle concentration at leading order $c(x, y)$ by using the first boundary condition in (44) along with (52), to obtain

$$c = \exp\left\{-\int_0^y \left[\lambda_f \frac{\phi^{\frac{1}{2}}}{v} + \delta_f \Big(1 - \phi^{\frac{1}{2}}\Big)\right] dy'\right\}. \tag{53}$$

Furthermore, (53) is used in (45) to find an initial value problem for the leading order of porosity $\phi(x, y, t)$,

$$\frac{\partial \phi}{\partial t} = -\big[\alpha_f \phi^{\frac{1}{2}} + v\big(1 - \phi^{\frac{1}{2}}\big)\big] c, \quad \phi(x, y, 0) = \phi_{f_{\text{initial}}}(x, y). \tag{54}$$

Note that (54) can be simply solved by forward Euler's method. Finally, by using (52), the leading order of the dimensionless flux $\mathcal{Q}(t)$ and throughput $\mathcal{V}(t)$ given in (46) are obtained as

$$\mathcal{Q} = \int_0^1 v\,dx, \quad \mathcal{V} = \int_0^t \mathcal{Q}\,dt'. \tag{55}$$

All integrals in (52), (53), and (55) are calculated by using trapezoidal quadrature.

B. Drying

In the context of the drying process, we consider two distinct scenarios based on the role of particle dispersion in the system dynamics. The first case addresses the interplay between particle dispersion and deposition, and the second case focuses on the scenario where particle deposition is the dominant effect in the drying process.

1. Case I: The drying model includes the particle dispersion and deposition terms.

Under the assumptions $T_d = \mathcal{O}(1)$ and $\lambda_d = \mathcal{O}(1)$, Eqs. (47) and (48) form the initial boundary value problem for $\beta(x, y, t)$ in the fluid region Ω_f,

$$T_d \frac{\partial \beta}{\partial t} = \frac{\partial^2 \beta}{\partial y^2} - \lambda_d \phi^{\frac{1}{2}} \left(\frac{\beta}{\phi} - c_{\text{sat}} \right)_+, \quad \frac{\partial \beta}{\partial y}\bigg|_{y=h_i(x)} = \pm \gamma_d E \beta, \quad i \in \{T, B\}, \quad \beta|_{t=0} = \beta_{d_{\text{initial}}}. \tag{56}$$

From (49) and (50), the motion of the top and bottom dry-fluid interfaces $h_{T,B}(x, t)$ is governed by

$$\frac{\partial h_T}{\partial t} = \eta_d E, \quad h_T|_{t=0} = 0, \quad \frac{\partial h_B}{\partial t} = -\eta_d E, \quad h_B|_{t=0} = 1, \quad \text{where} \quad E = \frac{\phi^2}{\phi + \Psi \beta}. \tag{57}$$

Finally, from (51) the leading-order dynamics of porosity $\phi(x, y, t)$ in the fluid region Ω_f is governed by the initial value problem

$$\frac{\partial \phi}{\partial t} = -\alpha_d \phi^{\frac{1}{2}} \left(\frac{\beta}{\phi} - c_{\text{sat}} \right)_+, \quad \phi|_{t=0} = \phi_{d_{\text{initial}}}. \tag{58}$$

2. Case II: The drying model does not include the particle dispersion term.

Under the assumption $T_d \gg 1$ and $\lambda_d / T_d = O(1)$, particle dispersion becomes negligible during the drying process, and the initial boundary value problem (56) reduces to a simplified initial value problem,

$$\frac{\partial \beta}{\partial t} = -\tilde{\lambda}_d \phi^{\frac{1}{2}} \left(\frac{\beta}{\phi} - c_{\text{sat}} \right)_+, \quad \beta|_{t=0} = \beta_{d_{\text{initial}}}, \tag{59}$$

where $\tilde{\lambda}_d = \lambda_d / T_d$ is a rescaled deposition coefficient. The governing equations for the dry-fluid interfaces and porosity, (57) and (58), remain unchanged.

Next, we discuss the numerical method to solve the system (56)–(58) for the drying process in Case I. Starting from the initial porosity and particle concentration profiles specified in (56) and (58), we iteratively solve the leading-order equations (56) and (58) for $\beta(x, y, t)$ and $\phi(x, y, t)$ in the fluid region Ω_f with moving boundaries $h_T(x, t)$ and $h_B(x, t)$, which are governed by the equations (57). Given dry-fluid interfaces $h_T(x, t^n)$ and $h_B(x, t^n)$, as well as (β, ϕ) at the time step $t = t^n$, where $t^n = n\Delta t$ and Δt is the time increment, we solve (56) and (58) for (β, ϕ) at the new time step $t = t^{n+1}$. Centered finite differences and implicit-explicit time stepping scheme are used for equation (56), where the dispersion term $\partial^2 \beta / \partial y^2$ is treated implicitly and the deposition term $\lambda_d \phi^{1/2} (\beta/\phi - c_{\text{sat}})_+$ is treated explicitly. The equation (58) is solved by using forward Euler time stepping. The updated $\phi(x, y, t^{n+1})$ and $\beta(x, y, t^{n+1})$ at the interfaces are then used to evaluate the leading order of the evaporative flux E given in (57). Finally, we solve the evolution equation (57)

TABLE I. Dimensional parameter values (V. Venkateshwaran, private communication (2017); see also Refs. [9,44]).

Parameter	Description	Typical value and units
$\hat{H}$	Membrane thickness	2×10^{-4} m
$\hat{L}$	Membrane length	0.2 m
$\hat{\mu}$	Viscosity of feed	10^{-3} kg m^{-1} s^{-1}
$\hat{P}_{\text{inlet}}$	Pressure drop across membrane	10^{5} kg m^{-1} s^{-2}
$\hat{\chi}$	Kozeny coefficient (characteristic membrane permeability)	10^{-16} m^{2}
$\hat{c}_{\text{inlet}}$	Total concentration of particles in feed suspension	10^{-3} mol m^{-3}
$\hat{\Xi}$	Dispersion coefficient of particles in feed suspension	10^{-11} m^{2} s^{-1}
$\hat{\alpha}_f$	Pore shrinkage coefficient, see (8)	0.125 mol^{-1} m^{3}
$\hat{\lambda}_f$	Average adsorption rate of particles, see (10)	0.01–4 s^{-1}
$\hat{\delta}_f$	Average blocking coefficient, see (10)	4×10^{4} m^{-1}
$\hat{\gamma}_d$	Scaling parameter for particle deposition rate, see (16)	2 (unitless)
$\hat{\eta}_d$	Evaporation coefficient, see (21)	2.5×10^{-8} m s^{-1}
$\hat{\alpha}_d$	Pore shrinkage coefficient, see (22)	10^{4} mol^{-1} m^{3}
$\hat{\lambda}_d$	Average adsorption rate of particles, see (24)	10^{-5}–4 s^{-1}
$\hat{c}_{\text{sat}}$	Saturation concentration of particles	10^{-4} mol m^{-3}

using the forward Euler time-stepping scheme to obtain the dry-fluid interfaces $h_T(x, t^{n+1})$ and $h_B(x, t^{n+1})$ at the new time step $t = t^{n+1}$. For the drying model without particle dispersion, as outlined in Case II, we apply a similar numerical scheme, with the exception that the governing equation (59) for β is solved by a forward Euler method.

VI. RESULTS

In this section, we numerically investigate the models for filtration and drying processes in filter membranes in Secs. VI A and VI B, respectively. Inspired by industrial applications, in Sec. VI C, we also study the evolution of the membrane structure over several filtration-drying cycles by coupling the filtration and drying models in time.

Our models involve system parameters that are estimated based on the typical ranges arising in filtration-drying applications. The values of these parameters depend on physical dimensional parameters that must be measured for the particular system under investigation, and in many cases reliable data are lacking. Instead of conducting an exhaustive investigation of the impacts of all parameters [13], we rely on our best judgment to determine the most suitable values to use in simulations. The parameters are summarized in Tables I (dimensional parameters) and II (dimensionless parameters) along with typical values, where known. Although a high level of variability and uncertainty in parameter values is noted, in practice users and filter membrane manufacturers should be able to work together to provide values or estimates for most of the parameters listed in Table I for specific applications. These values are dependent on physical characteristics of the filter membrane and the feed fluid. Certain other parameters, such as the average adsorption rate of particles in the filtration and drying processes, denoted by $\hat{\lambda}_f$ and $\hat{\lambda}_d$, respectively, are more difficult to estimate and will require preliminary experiments. Methods such as fluorescence microscopy (see Jackson *et al.* [45]), with particles in the feed suspension fluorescently tagged, can be used to estimate the values of $\hat{\lambda}_f$ and $\hat{\lambda}_d$. By comparing solutions of (43) and (56) with experimental images that reveal the density and location of particles trapped within the filter, one can arrive at a reliable estimate of these parameters.

To capture the overall evolution of the dry-fluid interfaces, it is useful to define an effective evaporation rate based on the averaged evaporative flux over the top and bottom dry-fluid interfaces,

TABLE II. Dimensionless parameter definitions and range of values used.

Parameter	Formula and description	Typical value
ϕ_{initial}	Initial average porosity (void fraction)	0.5–0.7
T_f	$\epsilon\hat{L}\hat{\alpha}_f\hat{\delta}_f\hat{c}_{\text{inlet}}$ Ratio of rates of pore-blocking and advective particle transport	Assumed asymptotically small
Pe	$(\hat{\chi}\hat{p}_{\text{inlet}})/(\hat{\Xi}\hat{\mu})$ Ratio of advective and dispersive particle transport (Peclet number)	Assumed asymptotically large
λ_f	$(\epsilon^2\hat{L}^2\hat{\mu}\hat{\lambda}_f)/(\hat{\chi}\hat{p}_{\text{inlet}})$ Ratio of rates of particle adsorption and advective particle transport (deposition coefficient)	1
δ_f	$\epsilon\hat{L}\hat{\delta}_f$ Blocking coefficient (δ_f^{-1} measures penetrative potential of blocking particles in depth of membrane)	8
α_f	$(\epsilon\hat{L}\hat{\mu}\hat{\lambda}_f)/(\hat{\delta}_f\hat{\chi}\hat{p}_{\text{inlet}}) = \lambda_f/\delta_f$	0.125
c_{sat}	$\hat{c}_{\text{inlet}}/\hat{c}_{\text{sat}}$	0.1
T_d	$(\epsilon\hat{L}\hat{\alpha}_f\hat{\delta}_f\hat{\chi}\hat{p}_{\text{inlet}}\hat{c}_{\text{inlet}})/(\hat{\Xi}\hat{\mu}) = T_f\text{Pe}$ Ratio of rates of pore-blocking and dispersive particle transport	1
λ_d	$(\epsilon^2\hat{L}^2\hat{\lambda}_d)/\hat{\Xi}$	0.1
γ_d	$(\epsilon\hat{L}\hat{\gamma}_d\hat{\eta}_d)/\hat{\Xi}$	1
η_d	$(\hat{\mu}\hat{\eta}_d)/(\hat{\alpha}_f\hat{\delta}_f\hat{\chi}\hat{p}_{\text{inlet}}\hat{c}_{\text{inlet}})$ Evaporation parameter	0.1–0.8
α_d	$(\epsilon\hat{L}\hat{\mu}\hat{\alpha}_d\hat{\lambda}_d)/(\hat{\alpha}_f\hat{\delta}_f\hat{\chi}\hat{p}_{\text{inlet}})$	0.5–1
Ψ	$(\hat{\Psi}\hat{c}_{\text{inlet}})/\hat{c}_{\text{sat}}$	0.1

i.e.,

$$\bar{E}_i = \int_0^1 E(\phi, c)\,dx, \quad \text{at} \quad y = h_i(x), \quad i \in \{T, B\}. \tag{60}$$

We also define the average porosity and particle concentration in the fluid region as

$$\bar{\phi} = \int_0^1 \int_{h_T(x)}^{h_B(x)} \phi\,dy\,dx, \quad \bar{c} = \int_0^1 \int_{h_T(x)}^{h_B(x)} c\,dy\,dx. \tag{61}$$

The integrals in (60) and (61) are numerically evaluated using trapezoidal quadrature.

A. Filtration

We first numerically simulate the leading-order asymptotic model (52)–(54) for the filtration process, where the initial porosity profile is chosen to be

$$\phi_{f_{\text{initial}}}(x, y) = 0.8 - 0.2\tanh(y) + 0.03\sin(2\pi x). \tag{62}$$

This spatially varying initial porosity profile represents a typical filter membrane with higher and lower porosity near the membrane upstream and downstream sides, respectively. Such negative porosity gradient in the depth of the filter has been demonstrated to improve filter efficiency by using more porous structure to address intensive filter fouling near the upstream side [9,17]. While we present numerical results for the initial porosity profile (62), our discussions can be readily extended for filters with any initial porosity profiles.

For all the simulations for the filtration process in this paper, we set the dimensionless parameters $\lambda_f = 1$, $\delta_f = 8$, and $\alpha_f = \lambda_f/\delta_f = 0.125$. Figure 2(a) presents the dynamic evolution of the porosity ϕ and concentration c for $0 \leqslant t \leqslant 1$, showing that the porosity near the top region of the membrane significantly decays during the filtration process. We also observe that regions with

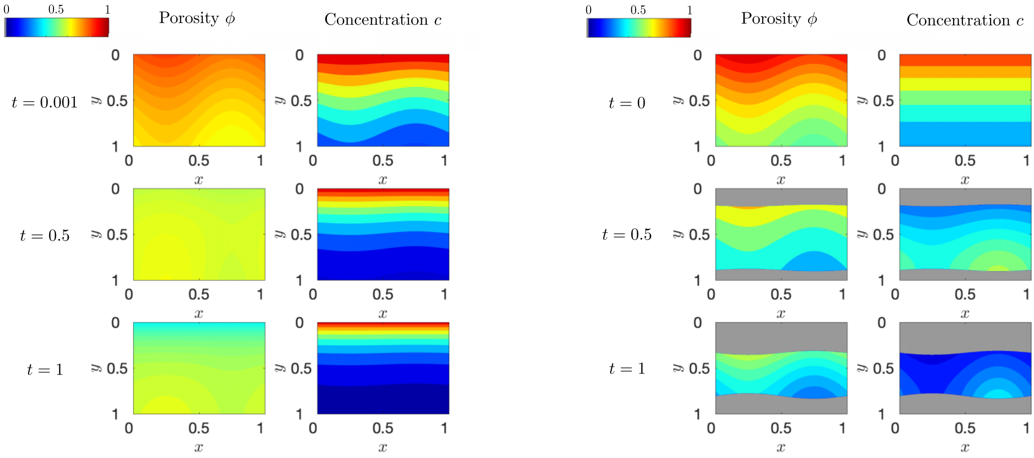

(a) Filtration process (b) Drying process

FIG. 2. Numerical simulations for filtration and drying processes. (a) Dynamic solution of the leading-order asymptotic model (52)–(54) for the filtration process starting from initial porosity defined in (62). The system parameters are $\lambda_f = 1$, $\delta_f = 8$, and $\alpha_f = \lambda_f/\delta_f = 0.125$. (b) Dynamic solution of the leading-order model (56)–(58) for the drying process starting from the initial porosity and particle concentration defined in (63). The system parameters are $c_{\text{sat}} = 0.1$, $T_d = 1$, $\lambda_d = 0.1$, $\gamma_d = 1$, $\eta_d = 0.5$, $\alpha_d = 1$, and $\Psi = 0.1$.

higher porosity have lower particle concentration. As the porosity ϕ attains its minimum near the top boundary of the membrane $y = 0$, the particle concentration c approaches 1. This implies that the porosity of regions that are exposed to higher particle concentration evolves more drastically.

B. Drying

Here we study and simulate the leading-order asymptotic model (56)–(58) for (β, ϕ, h) during the drying process, where $\beta = \phi c$. For simplicity, we fix the initial porosity profile and concentration and set

$$\phi_{d_{\text{initial}}}(x, y) = 0.9 - 0.5 \tanh y + 0.05 \sin(2\pi x), \qquad c_{d_{\text{initial}}}(x, y) = 0.9 - 0.8 \tanh y. \tag{63}$$

For all the simulations presented in this section, we set the dimensionless parameters $T_d = 1$, $\gamma_d = 1$, $c_{\text{sat}} = 0.1$, $\Psi = 0.1$, and $\lambda_d = 0.1$. In this section, we will focus on the influence of the evaporation coefficient η_d and the pore shrinkage coefficient α_d on the drying dynamics.

In Fig. 2(b), we present the evolution of the porosity ϕ and concentration c for the drying process with a moderate evaporation coefficient ($\eta_d = 0.5$). Here the gray area at the top and bottom of the membrane represents the dry region. The evolution of the dry-fluid interfaces $h_T(x,t)$ and $h_B(x,t)$ are governed by the local porosity and particle concentration at the interfaces. As shown in Fig. 2(b), at the early stage, the concentration c is nearly uniform in x, and the spatial variation in ϕ at the interface leads to spatially varying dry-fluid interfaces. Since the evaporative flux [see (57)] is proportional to the porosity ϕ, the dry-fluid interfaces h_T and h_B move at a faster speed in regions where the porosity ϕ is higher.

Figure 3(a) characterizes the effective evaporation rate at the top and bottom interfaces, $\bar{E}_T$ and $\bar{E}_B$, respectively [see (60)], as well as the average porosity and particle concentration in the fluid region $\bar{\phi}$ and $\bar{c}$ [see (61)], respectively. Since the porosity ϕ is much higher near the top interface than near the bottom interface, the effective evaporation rate $\bar{E}_T$ is significantly larger than $\bar{E}_B$ during the evolution. Moreover, Fig. 3(a) shows that due to excessive particle deposition during the drying process, both of the average porosity $\bar{\phi}$ and the average particle concentration $\bar{c}$ defined in (61) decrease in time.

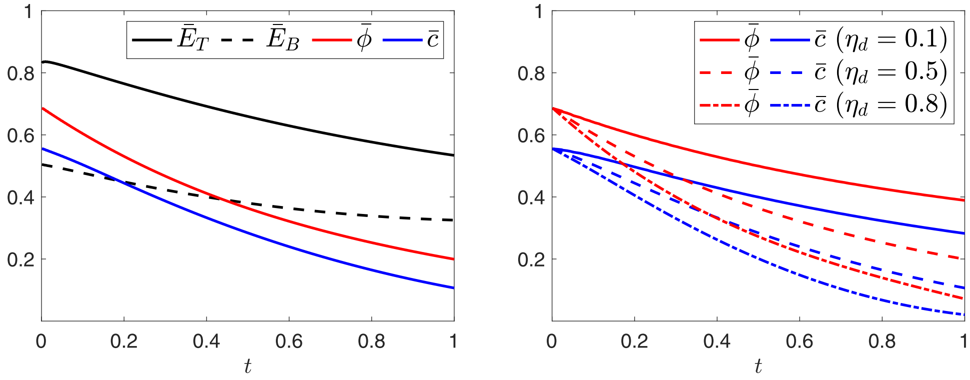

(a)

(b)

FIG. 3. (a) Plots of the effective evaporation rates ($\bar{E}_T$, $\bar{E}_B$) at the dry-fluid interfaces, as well as the average porosity and particle concentration ($\bar{\phi}$, $\bar{c}$), respectively, in the fluid region versus time t, corresponding to the drying process shown in Fig. 2(b). (b) The average porosity and particle concentration ($\bar{\phi}$, $\bar{c}$), respectively, for several values of the evaporation coefficient η_d. The other parameters are identical to those use in Fig. 2(b). In (a) we have $\eta_d = 0.5$, and for both (a) and (b) we set $\gamma_d = 1$, $T_d = 1$, $\alpha_d = 1$, $c_{\text{sat}} = 0.1$, $\Psi = 0.1$, and $\lambda_d = 0.1$.

The parameter η_d appeared in (57) scales the evaporation flux through the two dry-fluid interfaces. To study the effects of η_d, we simulate the drying process with varying η_d while keeping the other parameters and the initial conditions identical to those in Fig. 2(b). In Fig. 3(b), we present the influence of the parameter η_d on the average porosity $\bar{\phi}(t)$ and particle concentration $\bar{c}(t)$ in the fluid region. Our results with $\eta_d = 0.1, 0.5, 0.8$ show that with stronger evaporation effects ($\eta_d = 0.8$), both $\bar{\phi}(t)$ and $\bar{c}(t)$ in the fluid region decrease at a faster rate in time t. The pore shrinkage coefficient α_d in (58) is an important parameter in analyzing the dynamics of the drying process. In Fig. 4(a), we use the drying model in Case I given by (56)–(58) to plot the average porosity in the x direction $\langle\phi\rangle_x = \int_0^1 \phi(x, y)\, dx$ at the intial time $t = 0$ as well as the final time $t = 1$ for different values of α_d ($\alpha_d = 0.5, 0.8, 1$), while keeping the other system parameters and initial configurations identical to those used in Fig. 2(b). The initial average porosity in the x direction at time $t = 0$ is plotted in a

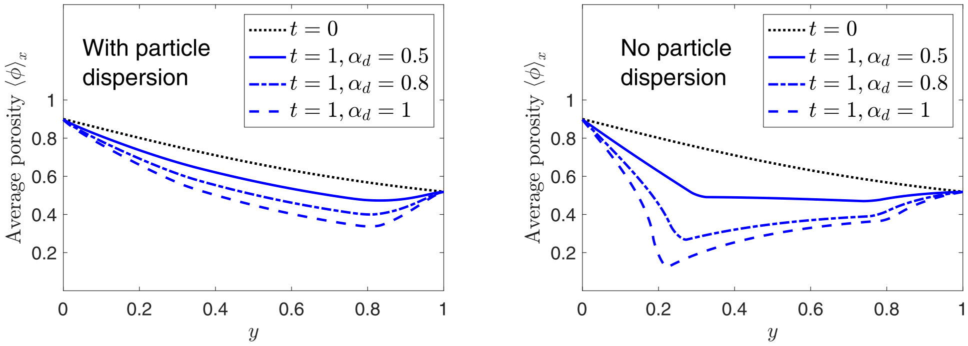

(a)

(b)

FIG. 4. The average porosity in the x direction, $\langle\phi\rangle_x(y) = \int_0^1 \phi(x, y)\, dx$, at times $t = 0$ (black dotted curve) and $t = 1$ for several values of the pore shrinkage coefficient $\alpha_d = 0.5, 0.8, 1$. Panel (a) shows the results obtained by solving the drying system in Case I (56)–(58); panel (b) corresponds to the results from the reduced system in Case II (57)–(59) where $\tilde{\lambda}_d = 0.1$. The other parameters are identical to those used in Fig. 2(b).

black dotted curve. Here we observe that the combined effects of evaporation, particle dispersion, and particle deposition lead to a decreased x-direction average porosity profile at the final time $t = 1$. Moreover, a larger value of the pore shrinkage parameter α_d corresponds to a stronger particle deposition rate, lowering $\langle \phi \rangle_x$ more significantly. Figure 4(a) also shows that the average porosity $\langle \phi \rangle_x$ at the top and bottom membrane boundary, $y = 0$ and $y = 1$, does not change in time. This is due to the fact that the interaction between the particles and the membrane only occurs in the fluid region, and the dry-fluid interfaces $y = h_i(x)$, $i \in \{T, B\}$ move away from the membrane boundary immediately at $t = 0$ as evaporation occurs.

When particle dispersion is negligible during the drying process (as outlined in Case II), the evolution of porosity and concentration in the fluid region is governed by the reduced system (57)–(59). Figure 4(b) shows the average porosity in the x direction over time obtained by solving the reduced system, while keeping all other settings identical to those used in Fig. 4(a). Comparing Fig. 4(a) and Fig. 4(b) reveals that particle dispersion can significantly slow down the decay in material porosity near the top dry-fluid interface. For the rest of this study, we will concentrate on the drying model that takes into account the presence of particle dispersion.

C. Filtration-drying cycles

In many industrial applications, filter membranes can be reused several times during their lifetime, while their performance deteriorates. Motivated by this, we monitor the membrane porosity evolution during coupled filtration and drying cycles to find out how long a filter membrane can be used before it becomes ineffective. Starting with a membrane of the prescribed initial porosity given in (62), the system undergoes a filtration process, during which the deposited particles in the porous medium reduces the membrane porosity. This is followed by a drying process, during which the evaporation takes place and governs the evolution of dry-fluid interfaces. The membrane porosity also changes due to the particle dispersion and deposition. After completing a full filtration-drying cycle, the membrane with reduced porosity will be used again for another cycle.

By coupling the filtration model (52)–(55) and the drying model (56)–(58) in time t, we construct a filtration-drying cycle model to characterize the evolution of a membrane filter. A complete filtration-drying cycle starting from time $t = t_0$ consists of a filtration process from time $t = t_0$ to time $t = t_0 + \Delta\mathcal{T}_f$, followed by a drying process to time $t = t_0 + \Delta\mathcal{T}_f + \Delta\mathcal{T}_d$. For simplicity, we assume that the filtration and drying processes have the same length of period, $\Delta\mathcal{T}_f = \Delta\mathcal{T}_d = \Delta\mathcal{T}$; however, our model and analysis can be readily extended to more general scenarios. The initial porosity for the filtration process [see (54)] is specified by the initial porosity of an unused filter or the porosity profile obtained from the previous filtration-drying cycle. After simulating the filtration process by solving the filtration model (52)–(55), we then apply the particle concentration c and the reduced porosity ϕ at time $t = t_0 + \Delta\mathcal{T}$ to construct the initial conditions for the drying model (56)–(58). The updated membrane porosity at the end of the drying process at time $t = t_0 + 2\Delta\mathcal{T}$ is then used as the initial condition for the next cycle of the filtration process.

To determine the lifespan of the filter membrane, in practice, it is crucial to trace key membrane properties and performance metrics such as the flux $\mathcal{Q}(t)$ and throughput $\mathcal{V}(t)$ defined in (55) over the filtration-drying cycle. Figure 5(a) presents the flux $\mathcal{Q}(t)$ and the throughput $\mathcal{V}(t)$ in time t for a filter membrane undergoing three filtration-drying cycles from $t = 0$–2, $t = 2$–4, and $t = 4$–6, where the length of each individual filtration and drying process is $\Delta\mathcal{T} = 1$. The initial porosity for the first filtration-drying cycle is set as in (62). The flux $\mathcal{Q}(t)$ drops significantly after each filtration process, and the flux $\mathcal{Q} = 0$ during the drying processes after each filtration process halts. The throughput $\mathcal{V}(t)$ increases with time and reaches a plateau after the third cycle completes, indicating that the filter performance dramatically drops after three cycles and reusing the filter for another cycle becomes ineffective.

The throughput-flux relation over multiple cycles also depends on the evaporation parameter during the drying process. Figure 5(b) represents the flux-throughput curves over three filtration-drying cycles for several values of the evaporation coefficient η_d. This figure shows that the flux-throughput

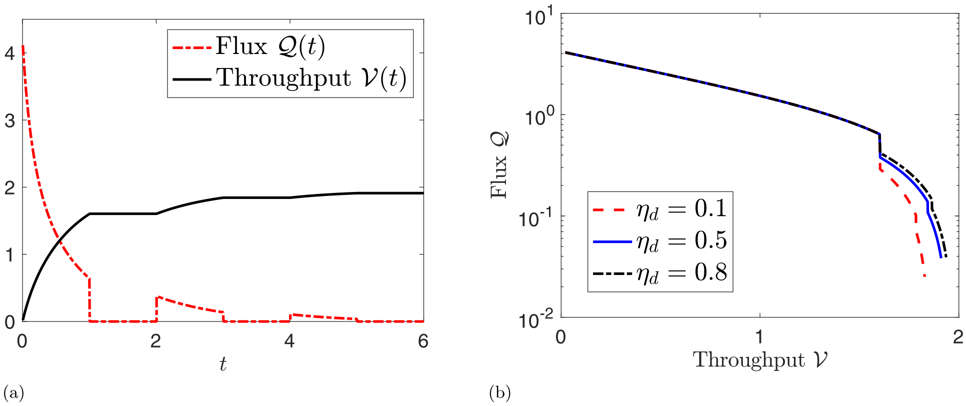

FIG. 5. (a) Plots of flux $\mathcal{Q}(t)$ and throughput $\mathcal{V}(t)$ in time over three filtration-drying cycles with the initial porosity profile given in (62). The evaporation parameter $\eta_d = 0.5$ and the length of individual filtration/drying period $\Delta\mathcal{T} = 1$. (b) The flux-throughput curves over three filtration-drying cycles for several values of the evaporation coefficient η_d. Other system parameters are identical to those used in Fig. 2.

relation is sensitive to the evaporation parameter η_d. With the presence of weak evaporation effects ($\eta_d = 0.1$), more particles are deposited in the fluid region during the drying process, which leads to further reduced membrane porosity and a slightly faster decrease in the flux $\mathcal{Q}$. Note that in Fig. 5 other system parameters are chosen to be identical to those used in Fig. 2.

To further investigate the porous medium internal morphology evolution over multiple cycles, we perform a sequence of numerical simulations starting from identical initial filter porosity given in (62) over several filtration-drying cycles, where the number of cycles $N_{\text{cycle}} = 1, 2, \ldots, 5$. For each study with a fixed N_{cycle}, we also vary the length of individual filtration/drying period $\Delta\mathcal{T}$ and track the overall throughput $\mathcal{V}_{\text{overall}}$ after N_{cycle} complete cycles, where the overall throughput is defined by $\mathcal{V}_{\text{overall}} = \mathcal{V}(t = 2N_{\text{cycle}}\Delta\mathcal{T})$. Figure 6 presents the overall throughput $\mathcal{V}_{\text{overall}}$ as a function of $\Delta\mathcal{T}$, where $0.02 \leqslant \Delta\mathcal{T} \leqslant 1$. It shows that with a fixed number of N_{cycle}, the overall throughput $\mathcal{V}_{\text{overall}}$ increases with $\Delta\mathcal{T}$, and the curves become more flattened with larger values of $\Delta\mathcal{T}$. Similarly, for

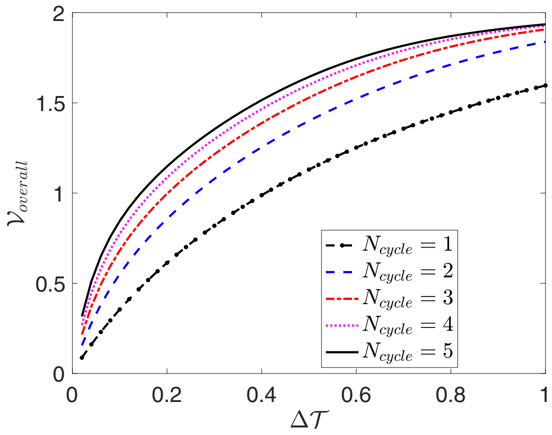

FIG. 6. A plot of the final throughput $\mathcal{V}_{\text{overall}}$ as a function of $\Delta\mathcal{T}$, after a varying number coupled filtration and drying cycles, showing the dependence of the filter performance on the length of individual filtration/drying period $\Delta\mathcal{T}$ and the total number of cycles N_{cycle}. The initial porosity is given by (62). The system parameters are identical to those used in Fig. 2.

a fixed $\Delta\mathcal{T}$, the overall throughput $\mathcal{V}_{\text{overall}}$ also increases with the number of cycles N_{cycle}. This observation indicates that while both N_{cycle} and $\Delta\mathcal{T}$ contribute positively to the overall throughput, using the filter membranes for too many cycles or unnecessarily extending the length of individual process only marginally increases the overall throughput. This analysis provides insights to the trade-off between the lifespan of filter membranes and their overall performance. Based on the prediction of the overall throughput over multiple cycles, one may optimize the filtering process over N_{cycle} and $\Delta\mathcal{T}$ and decide when to discard the filter based on its optimum performance.

VII. DISCUSSION AND CONCLUSIONS

We have developed a comprehensive macroscopic model for the filtration and drying processes in a thin filter membrane, where the key elements include particle transport and deposition, solvent evaporation, and the morphological changes to the porous media. Specifically, for the drying process, our model describes how the dry-fluid interfaces evolve across the porous media and predicts how the particle deposition changes the media porosity. In addition, we model the filtration and drying processes both occurring in consecutive cycles until the membrane performance deteriorates. With that our reduced model provides insights into the overall porous medium evolution over cycles of filtration and drying processes, allowing us to predict the timeline for discarding the filter based on its optimum performance. We have observed interesting pattern formation in the media porosity and particle concentration from the coupled filtration and drying models, which provides insights to the performance of the porous media structure over multiple cycles.

Given the complexity of the membrane structure, the chemical interactions between the filtrate particles and the membrane material, and the evaporation conditions that highly depend on the application, our simplified model necessarily contains several parameters that could be difficult to measure for a particular membrane-evaporation system. In future, we plan to further study the dynamics predicted by the coupled model with parameter values appropriate for typical solvent and porous media structures provided by experimentalists in industry. We also note that our model does not incorporate the impact of thermal gradients, capillary forces, and wettability of the material to the evaporation fronts. It is of interest to develop a multiscale drying model for porous media that incorporates both the macroscopic and pore-level modeling approaches [22,29,30] in appropriate experimental settings.

In this paper, we focus on the two-dimensional filtration-drying model, and we expect some of the results can be naturally extended to three-dimensional cases, where more complex morphological changes to the membrane geometry and the evaporation fronts should be considered. It would also be of interest to incorporate the evaporation dynamics into more recently developed network-based models [46,47] for porous media flows, where the membrane filters are modeled by networks of connected pores.

ACKNOWLEDGMENTS

P.S. gratefully acknowledges support from the National Science Foundation (NSF) under Grant No. DMS-2108161. H.J. acknowledges support from Faculty Research and Professional Development Program (FRPD) from North Carolina State University. The work carried out in this paper arose from a problem presented at the 2021 Mathematical Problems in Industry workshop, held at University of Vermont and University of Delaware supported by NSF under Grants No. DMS 1916281 and No. 2016095.

[1] M. Aboufoul, N. Shokri, E. Saleh, C. Tuck, and A. Garcia, Dynamics of water evaporation from porous asphalt, Constr. Build. Mater. **202**, 406 (2019).

[2] N. Shokri, P. Lehmann, and D. Or, Effects of hydrophobic layers on evaporation from porous media, Geophys. Res. Lett. **35**, L19407 (2008).

[3] S. M. S. Shokri-Kuehni, T. Vetter, C. Webb, and N. Shokri, New insights into saline water evaporation from porous media: Complex interaction between evaporation rates, precipitation, and surface temperature, Geophys. Res. Lett. **44**, 5504 (2017).

[4] J. R. Philip, Evaporation, and moisture and heat fields in the soil, J. Atmos. Sci. **14**, 354 (1957).

[5] J. Van Brakel, Mass transfer in convective drying, Advances in Drying **1**, 217 (1980).

[6] P. Lehmann, S. Assouline, and D. Or, Characteristic lengths affecting evaporative drying of porous media, Phys. Rev. E **77**, 056309 (2008).

[7] T. Metzger and E. Tsotsas, Influence of pore size distribution on drying kinetics: A simple capillary model, Drying Technol. **23**, 1797 (2005).

[8] Z. Chen, S. Y. Liu, I. C. Christov, and P. Sanaei, Flow and fouling in elastic membrane filters with hierarchical branching pore morphology, Phys. Fluids **33**, 062009 (2021).

[9] D. Fong, L. J. Cummings, S. J. Chapman, and P. Sanaei, On the performance of multilayered membrane filters, J. Eng. Math. **127**, 23 (2021).

[10] D. Persaud, M. Smirnov, D. Fong, and P. Sanaei, Modeling of the effects of pleat packing density and cartridge geometry on the performance of pleated membrane filters, Fluids **6**, 209 (2021).

[11] B. Gu, D. L. Renaud, P. Sanaei, L. Kondic, and L. J. Cummings, On the influence of pore connectivity on performance of membrane filters, J. Fluid Mech. **902**, A5 (2020).

[12] Y. Sun, P. Sanaei, L. Kondic, and L. J. Cummings, Modeling and design optimization for pleated membrane filters, Phys. Rev. Fluids **5**, 044306 (2020).

[13] P. Sanaei and L. J. Cummings, Membrane filtration with multiple fouling mechanisms, Phys. Rev. Fluids **4**, 124301 (2019).

[14] E. Iritani, A review on modeling of pore-blocking behaviors of membranes during pressurized membrane filtration, Dry. Technol. **31**, 146 (2013).

[15] J. W. Chew, J. Kilduff, and G. Belfort, The behavior of suspensions and macromolecular solutions in crossflow microfiltration: An update, J. Membr. Sci. **601**, 117865 (2020).

[16] W. R. Bowen and F. Jenner, Theoretical descriptions of membrane filtration of colloids and fine particles: An assessment and review, Adv. Colloid Interface Sci. **56**, 141 (1995).

[17] P. Sanaei and L. J. Cummings, Flow and fouling in membrane filters: Effects of membrane morphology, J. Fluid Mech. **818**, 744 (2017).

[18] P. Sanaei, G. W. Richardson, T. Witelski, and L. J. Cummings, Flow and fouling in a pleated membrane filter, J. Fluid Mech. **795**, 36 (2016).

[19] P. Sanaei and L. J. Cummings, Membrane filtration with complex branching pore morphology, Phys. Rev. Fluids **3**, 094305 (2018).

[20] N. Shokri, Pore-scale dynamics of salt transport and distribution in drying porous media, Phys. Fluids **26**, 012106 (2014).

[21] M. Kvick, D. M. Martinez, D. R. Hewitt, and N. J. Balmforth, Imbibition with swelling: Capillary rise in thin deformable porous media, Phys. Rev. Fluids **2**, 074001 (2017).

[22] D. Panda, S. Paliwal, D. P. Sourya, A. Kharaghani, E. Tsotsas, and V. K. Surasani, Influence of thermal gradients on the invasion patterns during drying of porous media: A lattice boltzmann method, Phys. Fluids **32**, 122116 (2020).

[23] J. Thiery, S. Rodts, D. A. Weitz, and P. Coussot, Drying regimes in homogeneous porous media from macro-to nanoscale, Phys. Rev. Fluids **2**, 074201 (2017).

[24] L. Xu, S. Davies, A. B. Schofield, and D. A. Weitz, Dynamics of Drying in 3D Porous Media, Phys. Rev. Lett. **101**, 094502 (2008).

[25] F. Moebius and D. Or, Pore scale dynamics underlying the motion of drainage fronts in porous media, Water Resour. Res. **50**, 8441 (2014).

[26] P. Fantinel, O. Borgman, R. Holtzman, and L. Goehring, Drying in a microfluidic chip: Experiments and simulations, Sci. Rep. **7**, 15572 (2017).

[27] A. Scanziani, Q. Lin, A. Alhosani, M. J. Blunt, and B. Bijeljic, Dynamics of fluid displacement in mixed-wet porous media, Proc. R. Soc. A. **476**, 20200040 (2020).

[28] Z. Wang, K. Chauhan, J.-M. Pereira, and Y. Gan, Disorder characterization of porous media and its effect on fluid displacement, Phys. Rev. Fluids **4**, 034305 (2019).

[29] L. Cueto-Felgueroso, X. Fu, and R. Juanes, Pore-scale modeling of phase change in porous media, Phys. Rev. Fluids **3**, 084302 (2018).

[30] H. P. Huinink, L. Pel, M. A. J. Michels, and M. Prat, Drying processes in the presence of temperature gradients–pore-scale modelling, Eur. Phys. J. E **9**, 487 (2002).

[31] N. Vorhauer, E. Tsotsas, and M. Prat, Temperature gradient induced double stabilization of the evaporation front within a drying porous medium, Phys. Rev. Fluids **3**, 114201 (2018).

[32] M. M. Sharma and Y. C. Yortsos, A network model for deep bed filtration processes, AIChE J. **33**, 1644 (1987).

[33] M. M. Sharma and Y. C. Yortsos, Fines migration in porous media, AIChE J. **33**, 1654 (1987).

[34] M. M. Sharma and Y. C. Yortsos, Transport of particulate suspensions in porous media: Model formulation, AIChE J. **33**, 1636 (1987).

[35] R. F. Probstein, *Physicochemical Hydrodynamics: An Introduction* (John Wiley & Sons, New York, 2005).

[36] G. I. Taylor, Dispersion of soluble matter in solvent flowing slowly through a tube, Proc. R. Soc. Lond. A **219**, 186 (1953).

[37] S. Y. Liu, Z. Chen, and P. Sanaei, Effects of particles diffusion on membrane filters performance, Fluids **5**, 121 (2020).

[38] V. S. Ajaev and G. M. Homsy, Steady vapor bubbles in rectangular microchannels, J. Colloid Interface Sci. **240**, 259 (2001).

[39] V. S. Ajaev, Spreading of thin volatile liquid droplets on uniformly heated surfaces, J. Fluid Mech. **528**, 279 (1999).

[40] G. Karapetsas, K. C. Sahu, and O. K. Matar, Evaporation of sessile droplets laden with particles and insoluble surfactants, Langmuir **32**, 6871 (2016).

[41] R. V. Craster, O. K. Matar, and K. Sefiane, Pinning, retraction, and terracing of evaporating droplets containing nanoparticles, Langmuir **25**, 3601 (2009).

[42] J. Mahadevan, M. M. Sharma, and Y. C. Yortsos, Flow-through drying of porous media, AIChE J. **52**, 2367 (2006).

[43] J. Mahadevan, M. M. Sharma, and Y. C. Yortsos, Evaporative cleanup of water blocks in gas wells, SPE J. **12**, 209 (2007).

[44] D. Fong and P. Sanaei, Flow and transport in a pleated filter, Phys. Fluids **34**, 097102 (2022).

[45] N. B. Jackson, M. Bakhshayeshi, A. L. Zydney, A. Mehta, R. van Reis, and R. Kuriyel, Internal virus polarization model for virus retention by the Ultipor VF Grade DV20 membrane, Biotechnol. Progr. **30**, 856 (2014).

[46] B. Gu, L. Kondic, and L. J. Cummings, A graphical representation of membrane filtration, SIAM J. Appl. Math. **82**, 950 (2022).

[47] B. Gu, L. Kondic, and L. J. Cummings, Network-based membrane filters: Influence of network and pore size variability on filtration performance, J. Membr. Sci. **657**, 120668 (2022).